Super-resolution microscopy on single particles at fluid interfaces reveals their wetting properties and interfacial deformations†

A. Aloi, [ID] *[a,b,c] N. Vilanova,[a,c] L. Isa, [ID] [d] A. M. de Jong [ID] [a,e] and I. K. Voets [ID] *[a,b,c,f]

Solid particles adsorbed at fluid interfaces are crucial for the mechanical stability of Pickering emulsions. The key parameter which determines the kinetic and thermodynamic properties of these colloids is the particle contact angle, θ. Several methods have recently been developed to measure the contact angle of individual particles adsorbed at liquid–liquid interfaces, as morphological and chemical heterogeneities at the particle surface can significantly affect θ. However, none of these techniques enables the simultaneous visualization of the nanoparticles and the reconstruction of the fluid interface to which they are adsorbed, *in situ*. To tackle this challenge, we utilize a newly developed super-resolution microscopy method, called iPAINT, which exploits non-covalent and continuous labelling of interfaces with photo-activatable fluorescent probes. Herewith, we resolve with nanometer accuracy both the position of individual nanoparticles at a water–octanol interface and the location of the interface itself. First, we determine single particle contact angles for both hydrophobic and hydrophilic spherical colloids. These experiments reveal a non-negligible dependence of θ on particle size, from which we infer an effective line tension, τ. Next, we image elliptical particles at a water–decane interface, showing that the corresponding interfacial deformations can be clearly captured by iPAINT microscopy.

Introduction

Materials comprising homogeneous mixtures of immiscible fluids are of paramount importance for a broad range of natural and technological processes, but they all suffer from an unavoidable, thermodynamically driven propensity to phase-separate. One way to halt the macroscopic phase separ-

[a]Institute for Complex Molecular Systems, Eindhoven University of Technology, Post Office Box 513, 5600 MB Eindhoven, The Netherlands. E-mail: I.Voets@tue.nl, Antonio.Aloi@tue.nl

[b]Laboratory of Self-Organizing Soft Matter, Department of Chemistry and Chemical Engineering, Eindhoven University of Technology, Post Office Box 513, 5600 MB Eindhoven, The Netherlands

[c]Laboratory of Macromolecular and Organic Chemistry, Department of Chemistry and Chemical Engineering, Eindhoven University of Technology, Post Office Box 513, 5600 MB Eindhoven, The Netherlands

[d]Laboratory for Interfaces, Soft Matter and Assembly, Department of Materials, ETH Zurich, Vladimir-Prelog Weg 5, 8093 Zürich, Switzerland

[e]Laboratory of Molecular Biosensing, Department of Applied Physics, Eindhoven University of Technology, Post Office Box 513, 5600 MB Eindhoven, The Netherlands

[f]Laboratory of Physical Chemistry, Department of Chemistry and Chemical Engineering, Eindhoven University of Technology, Post Office Box 513, 5600 MB Eindhoven, The Netherlands

†Electronic supplementary information (ESI) available: Synthesis and characterization of particles, iPAINT data analysis, macroscopic characterization of the system, Fig.: S1–S19. See DOI: 10.1039/c8nr08633h

ation of two immiscible liquids makes use of the adsorption of micro- and nanoparticles at the fluid interface. It is the kinetic trapping of colloidal particles of various shape,[1–3] roughness,[4–6] softness,[7–11] and surface chemistry[12] at fluid interfaces, which grants long-term stability to particle-stabilized emulsions.[13,14] This enhances their mechanical properties and offers adequate protection against coalescence.[15–17]

Although particle-laden interfaces have been the subject of systematic investigations for more than a century,[13,14] only recently new methods have emerged as alternative to ensemble measurements to interrogate wetting properties at the single-particle level. The primary challenge for a precise estimation of the contact angle is the accurate localization of the adsorbed colloids and of the interface. Recent developments of methods with high spatial resolution and image contrast, such as interferometric microscopy,[18,19] freeze-fracture shadow-casting cryo-scanning electron microscopy (FreSCa),[5,20–22] digital holography,[23,24] Bessel beam microscopy,[25] and intra-pair magnetophoresis,[26,27] allowed directly observing single particles and measuring their vertical position with respect to the fluid interface. In addition to conventional contact-angle measurements, these new tools revealed that particle heterogeneities (*e.g.* chemical or shape anisotropies, surface functionalization, roughness) have a large impact on the stabilization of fluid interfaces.[5,28] In particular, one could finally extrapolate interfacial energy landscapes, and

pinpoint where particle detachments would be energetically more favoured,[25,29] and lead to mechanical instabilities.[30] Moreover, these could identify where particle dynamics would differ due to changes in local viscosity,[31–33] and when capillary forces would dominate assembly.[34,35]

These important insights illustrate the potential of the newly developed tools despite limitations in *e.g.* particle size and sample preparation. Some of the approaches require fixation of the (particles at the) interface to perform *ex situ* SEM or AFM imaging with nanometric spatial resolution. Fluid phases are for instance gelled and peeled-off in the gel trapping technique (GTT) to examine the particles' position,[36–38] which may perturb their equilibrium position at the interface due to the applied mechanical forces.[39] Moreover, GTT presents limited accuracy for objects smaller than 100 nm, since the gel's structural features are of the order of 10 nm. In an alternative approach, the position of the three-phase contact line (TPCL) is marked using specific chemical reactions for a more gentle identification.[40] The contact angle of single particles as small as 10 nm can be determined by FreSCa microscopy.[20,21,41,42] Its complex sample preparation comprises three steps of shock-freezing the fluid interface, exposing the particles upon fracturing the interface, and subsequently coating the colloids with a thin metal layer at a given metal-casting angle, α. FreSCa is well-suited for hydrophobic particles, but not for extremely hydrophilic particles with contact angles lower than the accessible range of metal-casting angles (*i.e.*, $\theta < \alpha_{cr}$, with $\alpha_{cr} = 30\text{–}45°$).[20] Moreover, a three-dimensional reconstruction of the interface surrounding the particles is not possible, and, as only part of the particles is visible, θ is extracted through geometrical assumptions on the particle shape.

Here, we present an innovative method which allows truly *in situ* imaging without any external fixation required of single, immobilized nanoparticles adsorbed at fluid interfaces and the simultaneous reconstruction of the interface to which they are adsorbed. To accomplish this, we exploit a single-molecule localization microscopy (SMLM)[43] technique known as interface Point Accumulation for Imaging in Nanoscale Topography (iPAINT), which was recently developed in our group.[44] This strategy exploits the interfacial adsorption of a photo-activatable dye end-attached to the water-soluble polymer polyethylene glycol (PEG-552) for the imaging of soft materials with <20 nm resolution (Fig. S2†).[45–48] Advantageously, iPAINT enables simultaneous visualization of both particles and interface *via* a simple, non-covalent staining approach; *i.e.*, physical adsorption of suitable dyes. Disadvantageously, this impacts the local force balance and hence affects *e.g.* the position of the particles at the interface, such that their contact angles are altered by ±10° (Fig. S12 and S13†).

We first demonstrate the visualization by iPAINT of the position of hydrophobic and hydrophilic spherical silica nanoparticles at the water–octanol interface. Next, we explore the wettability of the particles, determining their mean contact angles, θ, and related distributions. We find a non-negligible dependence of individual θ on particle's size that can be

ascribed to line tension effects. Finally, we image local deformations of the fluid interface induced by the adsorption of anisotropic particles. These findings demonstrate the potential of our innovative approach to advance the characterization and understanding of the role of particles on interface stabilization, which may aid the rational design of (nano)particles for Pickering emulsions.

Results and discussion

In situ imaging of colloidal particles at the interface between immiscible liquids

An accurate measurement of the wetting of individual particles adsorbed at fluid interfaces requires a precise localization of the particles' and interface's position. To critically evaluate whether iPAINT can be utilized for this purpose, we set out to image two extensively characterized systems:[49] plain hydrophilic and stearyl alcohol-grafted hydrophobic silica particles (Fig. S4 and S5†) at water–octanol interfaces. First, iPAINT probes (PEG-552) are solubilized in water and the colloids are dispersed in either the water or the oil phase, in accordance with their wettability. Next, water and oil droplets with the particles and iPAINT probes are placed side-by-side on a coverglass and subsequently compressed by a coverslip positioned on top to orient the water–oil interfaces normal to the coverslip, as schematically illustrated in Fig. 1a and b. This allows us to profit from the high accuracy in single molecule localization in the lateral plane (~17 nm). In the assembled sample chamber, a dynamic equilibrium is now established, wherein PEG-552 is predominantly solubilized in the aqueous phase and physically adsorbed at all the water-accessible interfaces (Fig. 1b): the water–oil interface, as well as the surface of the particles and the coverslip exposed to the water phase. To resolve the position of individual dyes with high precision, we tune the fraction of emitting dyes to several tens in a frame of ~1900 μm^2 by regulating the power of the photo-activation and the readout lasers (refer to Materials and Methods section, Fig. 1c and Fig. S1†). Conveniently, Brownian motion precludes PEG-552 localization in solution, while the individual labels are readily identified when adsorbed at interfaces where their motion is restricted (*i.e.*, particle surface, fluid interface and microscope coverslip).[44] Consequentially, all water-accessible interfaces are effectively stained. In a final step of image analysis, all single molecule localizations are summed up to yield a super-resolved reconstruction of the particles at the fluid interface.

An exemplary iPAINT image of a hydrophilic particle adsorbed at an octanol–water interface is presented in Fig. 2a. A pronounced difference in single-molecule localization density is apparent, which we exploit for unambiguous identification of the relevant interfaces. The stark contrast originates from the low respectively high solubility of PEG-552 in oil and water, which leads to an uneven partitioning between the two phases and the particle–water–octanol interfaces (the single-molecule localizations observed in the water and oil phase in
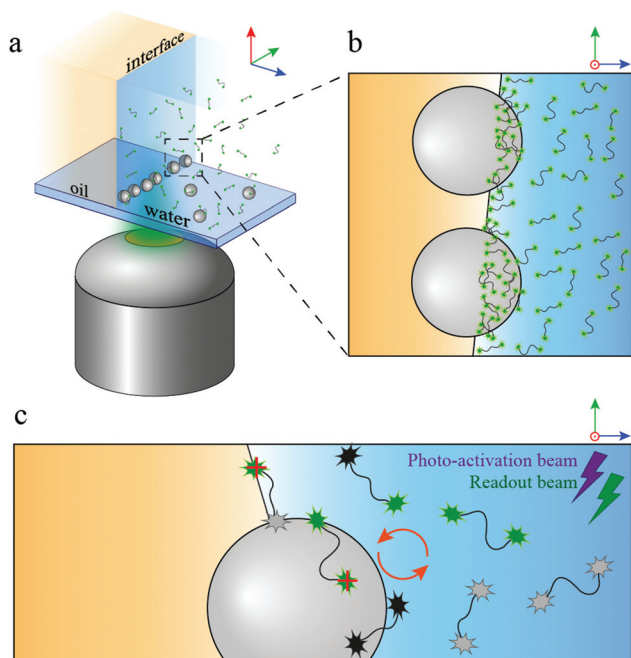
Fig. 1 iPAINT imaging of particles at a liquid–liquid interface. (a) 3D schematic of colloidal particles adsorbed at a water–oil interface illustrating the fluid interface normal to the microscope coverslip and focal plane. (b) Zoom-in of colloidal particles adsorbed at the oil–water interface. The water phase is enriched in PEG-552, while the amount of PEG-552 in the oil phase is negligible. As the probes absorb at interfaces, the water–oil interface, the water–coverslip interface and particle surfaces will be tagged. (c) Processes occurring in a typical iPAINT experiment: adsorption of caged (dark, non-fluorescent) iPAINT probes (grey stars) at solid and fluid interfaces, excited and ready to fluoresce probes (green stars), single probes localized (red crosses), bleached dye (black stars), and exchange of dye molecules between the reservoir and the interfaces (red arrows). Accumulating all localization points leads to the full reconstruction of the interfaces.

Fig. 2 Count-based identification of the position of the interface and the particles. (a) Super-resolved image of an oil–water interface. (b) Density of single-molecule localizations within the area limited by the dashed black line in (a) showing clear differences in PEG-552 localizations collected in the oil (yellow) and water (blue) phases, at the interface (green), and finally on the particle surface (red). (c) Single-molecule density per μm^2, averaged over more than 100 different samples prepared, in each of which oil phase, interface, water phase and particles have been calculated. (d) Single-molecule localizations identified in the black dashed area in (a) after applying suitable density parameters, according to the values in (c), and following sorting of single-molecule localizations.

Fig. 2a belong to the dye molecules adsorbed on the microscope coverslip). Additionally, particles and fluid interfaces show a different density of single-molecule localization being projected on a 2D plane. First, an area is selected, which spans both the octanol and water phases and is as wide as one and as long as fourteen particle diameters (700 nm × 10 μm, demarcated by a dashed line in Fig. 2a). Next, the density of single-molecule localizations per μm^2, $\delta_{SM\ loc.}$, is determined along the 10 μm cut (Fig. 2b) to obtain $\delta_{SM\ loc.}$ for the oil and water phases, the water–octanol interface, and both types of particles. The procedure is repeated for tens of measurements, which gives the averaged $\delta_{SM\ loc.}$ and associated standard deviations, as reported in Fig. 2c. These mean values are hereafter used as threshold parameters to discriminate between the four localization categories. These are subsequently split into four separate datasets in descending order of $\delta_{SM\ loc.}$ to analyse and display exclusively those localizations belonging to the particles (Fig. 2d, top row), the interface (Fig. 2d, second row), the water phase (Fig. 2d, third row), and the oil phase (Fig. 2d, bottom row). This procedure enables the localization with high
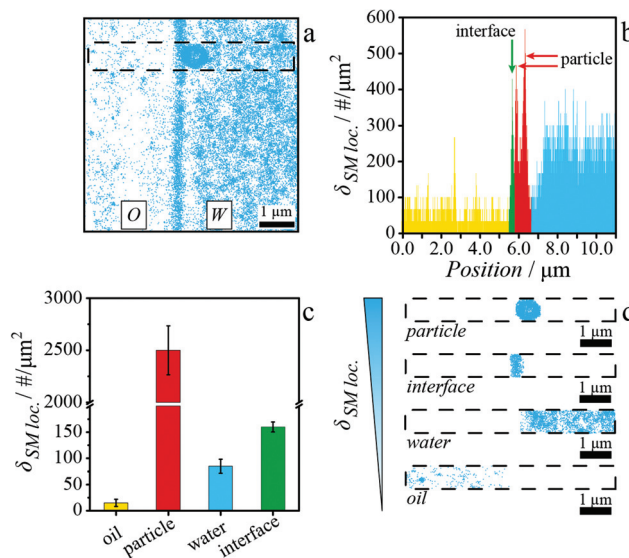
accuracy (<20 nm) of the position of both hydrophilic and hydrophobic particles relative to the interface (Fig. S6 and S7†).

Determining the contact angle of single hydrophilic and hydrophobic particles at an oil–water interface

The simultaneous visualization by iPAINT of spherical particles and the water–octanol interface to which they adsorb, enables the determination of the contact angle, θ, of single particles (Fig. 3).

To this end, the height of the spherical cap protruding through the interface, h, and its lateral dimension, $2l$, are obtained from iPAINT reconstructions in an analogous yet slightly different manner for hydrophilic and hydrophobic particles. Hydrophilic colloids are rather uniformly covered by PEG-552 (Fig. 3a and b), because these particles approached the interface from the aqueous phase. We therefore overlay the localization datasets belonging to the interface and to the particle to determine h and $2l$ (Fig. 3b and Fig. S6†). Hydrophobic particles, which were dispersed in octanol and thus approached the interface from the oil phase, are only partially labelled with PEG-552 where the particle surface has been exposed to water (Fig. 3d and e). Both h and $2l$ are thus directly determined from the localization datasets corresponding to the stearyl alcohol-coated beads (Fig. 3e and Fig. S7†). In line with the differences in surface functionalization and thus wett-
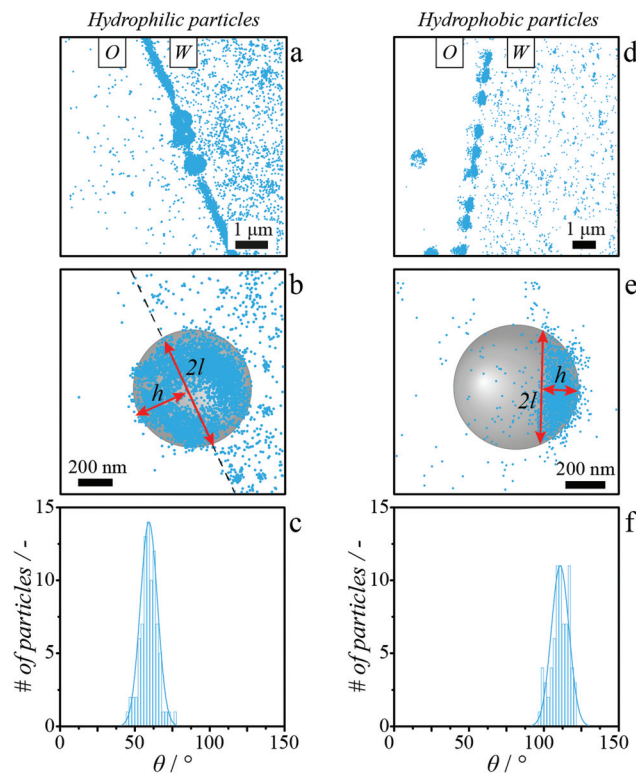
Fig. 3 iPAINT enables simultaneous and *in situ* visualization of particles at fluid interfaces. (a) Plain silica (hydrophilic) and (d) stearyl-alcohol coated (hydrophobic) silica particles adsorbed at the water–octanol interface. The water phase appears full of single molecule localizations (blue dots) while the oil phase is devoid of PEG-552, as it is primarily water-soluble. Hydrophilic particles are uniformly covered by PEG-552, while only the hemisphere wetted by the water phase is labelled for hydrophobic particles. (b, e) Zoom-ins of representative hydrophilic and hydrophobic colloidal particles, respectively. The grey sphere is a representation of a sphere with radius R = 330 nm. The black dashed line in (b) highlights the position of the oil–water interface. (c, f) Distribution of contact angles of hydrophilic and hydrophobic colloids, respectively.

ability of the two types of spherical particles with equal mean size, we obtain much smaller θ values for the hydrophilic particles (θ = 59.5° ± 6.9°, Fig. 3c) than for the hydrophobic particles (θ = 111.5° ± 7.0°, Fig. 3f). The single-particle values are also in agreement with the contact angles reported for μm-sized silica beads at water–octanol interfaces as obtained from ensemble measurements ($\theta_{hydrophilic}$ = 68° ± 6°,[49] $\theta_{hydrophobic}$ = 148° ± 5°,[49] and Fig. S14†). We observe a modest broadening of the contact angle distribution, σ_θ, due to particle size dispersity and possibly chemical heterogeneities of 5.5° and 2.3° for hydrophilic and hydrophobic particles, respectively (Fig. S9 and S10†). The interested reader is referred to the ESI† for an in-depth discussion of the computation of the single particle contact angles (eqn (S1) and (S3)†), aging of the TPCL (Fig. S8†),[50] and the impact of chemical heterogeneities, size dispersity[51] ($R_{hydrophobic}$ = 329 ± 21 nm, $R_{hydrophilic}$ = 328 ± 17 nm) and iPAINT experimental resolution (Fig. S9†) on σ_θ.

Recent single-particle experiments and simulations revealed that θ values for sub-μm particles at fluid interfaces scale line-

arly with particle size.[38] This is because θ values must be corrected for non-negligible contributions due to the line tension, τ, which corresponds to the force exerted on the particle around the TPCL.[38]

To evaluate the size-dependence of θ for hydrophilic and hydrophobic silica particles studied herein, we replot in Fig. 4 the single particle contact angle values as a function of their sizes. For clarity, θ values are averaged for particles differing less than 5 nm in mean radius (*i.e.*, $\Delta R_{bin} \leq 5$ nm, Fig. S11†). For hydrophobic particles (Fig. 4a), we recover the expected trend of increasing θ with increasing particle radius. Hydrophilic particles exhibit the opposite trend of increasing θ with decreasing particle radius (Fig. 4b). We may now compute τ from the iPAINT data using the Young–Dupré equation

$$\cos\,\theta = \cos\,\theta_{Young}\left[1 - \frac{\tau}{\gamma_{o/w}R\,\sin\,\theta}\right]^{-1}, \qquad (1)$$

with the surface tension between water and octanol $\gamma_{o/w}$ = 0.00852 N m^{-1}. We obtain an effective line tension in the order of 10^{-9} N, in agreement with previous experimental studies on single colloids at liquid interfaces.[20,21,36–38,50,52] These values are significantly higher than theoretical estimates, which predict forces in the 1–100 pN range.[39,53,54] The discrepancy could result from the presence of nanoscale surface heterogeneities, which lead to significantly longer contact lines compared to the idealized case of an unperturbed circular TPCL assumed in eqn (1). In this case, the Young–Dupré equation underestimates the effective contact line.

Visualizing local interfacial deformations induced by adsorbed elliptical particles

The *in situ* visualization of both adsorbed particles and liquid–liquid interfaces opens up the exciting prospect of imaging by iPAINT local deformations of the fluid interface induced by particle adsorption. To assess this possibility, we performed iPAINT experiments on ellipsoidal polystyrene particles (Fig. S15†) adsorbed at water–decane interfaces. It is well-known that such anisotropic particles distort the liquid–liquid interface to which they are adsorbed to locally satisfy Young's
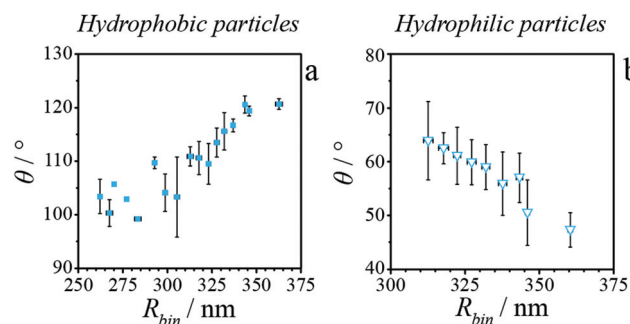

Fig. 4 Mean contact angles θ as function of averaged particle radius, R_{bin}, for (a) hydrophobic and (b) hydrophilic particles. Particle sizes differing less than 5 nm (*i.e.*, $\Delta R_{bin} \leq 5$ nm) are averaged. Error bars correspond to the standard deviation.

equation by pulling up the liquid along the major axis, and pushing it down at their tips (Fig. 5a).[55–58] Gratifyingly, local interfacial deformations around ellipsoids straddling a water-decane interface at the equilibrium position are indeed resolved by iPAINT (Fig. 5d and Fig. S16†). From iPAINT
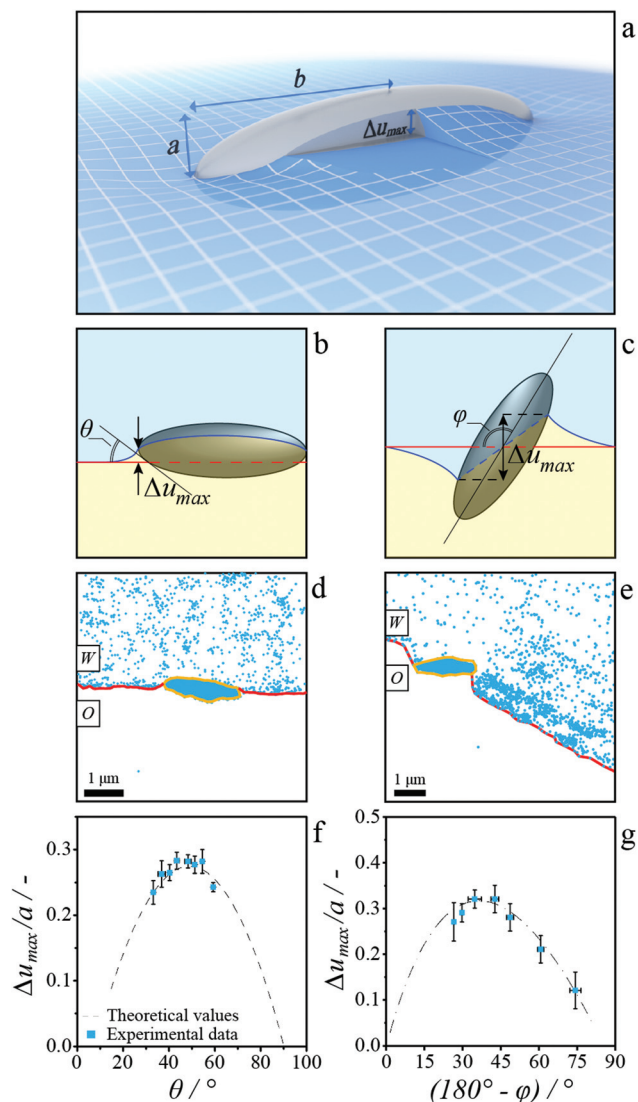
Fig. 5 Deformation of the oil–water interface due to the presence of anisotropic particles. (a) Schematic of deformations induced by an ellipsoidal particle at the equilibrium position straddling a fluid interface. Δu_{max} is the maximum displacement of the three-phase contact line. (b, c) Schematic showing the interfacial deformation (blue line) compared to an unperturbed interface (red line) for a (b) parallel and (c) tilted ellipsoid. (d, e) Exemplary iPAINT images of deformed fluid interfaces in presence of (d) parallel and (e) tilted ellipsoidal particles thereby adsorbed. The orange line along the ellipsoids perimeter and the red line used to define the fluid interface are determined by α-shaping.[62] Maximum difference in the contact line height, Δu_{max}, as a function of the (f) contact angle, θ, and of the (g) polar angle, φ, for parallel and oblique orientations of the ellipsoids, respectively. The dashed line in (f) shows the theoretical values from Dasgupta et al.[59] The dashed-dotted line in (g) is meant to guide the eye. The error bars represent the standard deviation.

images, we first determine the contact angle of single ellipsoids, θ (Fig. S18†), and then quantify the maximal interfacial deformation, Δu_{max}, at the tips of the particle (Fig. 5b). Δu_{max} is normalized by half the minor axis of each ellipsoid, a, to account for the dispersity in particle size. In agreement with theoretical predictions,[56,59] we find that Δu_{max} increases non-monotonically with θ (Fig. 5f) and goes to zero at 90° (dashed line in Fig. 5f). We find that Δu_{max} reaches a maximum value at $\theta = 43.4°$, in accordance with modelling studies by Lehle et al. and Dasgupta et al. predicting a maximum at $\theta = 46°$ (ref. 55) and $\theta = 48.5°$,[59] respectively.

Surprisingly, we also observe ellipsoids in an oblique orientation at fluid interfaces (Fig. 5e and Fig. S16, S17†). These particles are captured in a non-equilibrium state, which we define as an 'arrested configuration'. We speculate that this particular orientation occurs in our experiments as particles settle and are immobilized on the coverslip while pivoting within the interface towards their equilibrium position (Fig. S19†).

Simulations on ellipsoids with ferromagnetic dipoles in oblique orientations revealed a depression of the interface on one side and an elevation on the opposite side (Fig. 5c).[60,61] For a comparison of our findings with those results, we first define the tilting (polar) angle, φ, of the ellipsoid as the angle between the interface and the major axis of the colloid (Fig. S16†). We then determine the maximum deformation, Δu_{max}, which the interface can adopt as the distance along the surface normal between the outermost single-molecule localizations on the interface, close to the tips of the ellipsoid in the oil and in the water phase, respectively (Fig. 5c). In good agreement with computations,[63,64] this reveals a non-monotonic dependence of $\Delta u_{max}/a$ as a function of φ, which reaches a maximum at $\varphi = 38.7°$ and decreases to zero at $\varphi = 90°$ (Fig. 5g). These findings clearly demonstrate that iPAINT is a valuable complementary tool to visualize in situ colloidal particles at liquid–liquid interfaces as well as the interfacial deformations thereby induced, offering access to quantitative information on single particle contact angles and local interfacial perturbations.

Experimental

Materials and methods

Synthesis. 1.1 mg of poly(ethylene glycol) bis(amine) (MW 20 kDa, Sigma Aldrich) was set to react with 20 μL of 10 mM solution of N-hydroxysuccinimide ester activated rhodamine (Cage552, Abberior®) in 1 mL of 0.1 M sodium bicarbonate buffer at pH 8.5. The reaction mixture was stirred overnight, in the dark, and at room temperature. Subsequently the product was purified by dialysis (Spectra/Por®7 dialysis membrane, pre-treated RC tubing, molecular weight cutoff: 8 kDa) to remove unreacted dye molecules.

Hydrophilic silica beads of ~300 nm in radius were synthesized using a two-step Stöber-based method.[65] Silica particles with intermediate hydrophobicity were obtained by partially functionalizing them with stearyl alcohol through a

modified van Helden method (Fig. S4†).[66] Polystyrene ellipsoidal particles were obtained by stretching monodisperse sulfate latex spheres of 1 μm in diameter (Invitrogen) while embedded into a poly(vinyl alcohol) (PVA) matrix above the glass transition temperature and below the melting temperature of the material (Fig. S15†).[67] Here, prolate ellipsoids with aspect ratio of 5 were used.[22]

Sample preparation. Stock solutions of 0.6 mg mL^{-1} hydrophilic and hydrophobic particles were prepared by dispersion in 10^{-5} M aqueous solution of the iPAINT dye PEG-552 and octanol, respectively. For iPAINT imaging on the hydrophobic particles, a 15 μL droplet of the particle stock solution was placed onto a coverglass (Menzel Gläser, 76 × 26 mm, thickness 1 mm) next to a 15 μL droplet of aqueous solution of the iPAINT dye PEG-552 (10^{-5} M). The sample was sandwiched between the coverslide (Menzel Gläser, 76 × 26 mm, thickness 1 mm) and a coverslip (Menzel Gläser, No. 1.5, 24 × 24 mm, thickness 170 μm) using double-sided tape (∼90 μm). iPAINT imaging on hydrophilic beads was carried out similarly by placing a 15 μL droplet of pure octanol side by side to a 15 μL droplet of the hydrophilic silica beads dispersed in the iPAINT dye PEG-552 solution. Likewise, iPAINT imaging of ellipsoidal particles was carried out placing a 15 μL droplet of an aqueous solution of particles and iPAINT dye (10^{-4} M) next to a 15 μL droplet of decane. The sample chamber was assembled as described before. Prior to sample preparation, the coverslips were incubated for 10 min in a piranha solution (3 : 1 v/v concentrated $H_2SO_4 : H_2O_2$(aq. 30%)) to remove impurities, and reduce the background fluorescence. Solvent evaporation was not encountered during image acquisition due to the short imaging time-lapses (∼20 min for a 256 × 256 pixels field of view).

Being normal to the focal plane, and squeezed between two surfaces, the oil–water interface appeared μm-wide, depending on the angle of the *quasi*-total internal reflection fluorescence (TIRF) illumination adopted in the experiment. This is because the interfacial plane is not perfectly normal to the coverglass along the entire thickness of the spacers used. In other words, the interface is somewhat curved on μm length scale. However, the angle in the *quasi*-TIRF was set to illuminate the first μm's of the interface in contact with the coverslip. In this small penetration depth of the laser, we can assume that the interface is normal to the coverslip.

Limitations of the method. Accurate particle and interface localization by iPAINT necessitates gentle immobilization of both the particles and the interfaces. Drift of the particles or rearrangement of the liquid interface might lead to severe imaging artifacts. To this end, we first determine the position of the interface by wide-field imaging, and monitor its translation during the time-evolution of the sample towards the steady-state (Fig. S3†). iPAINT imaging is performed only after steady-state has been reached. Additionally, the adsorption of PEG-552 slightly alters the physico-chemical properties of the fluid–fluid interface. It imparts a change in the interfacial tension by acting as a surfactant; by covering the surface of the particles, PEG-552 alters the wettability of the colloids; the positive charge carried by the photo-activatable moiety alters the

particle-liquid surface tension. Overall, these factors will influence the measured contact angle. We estimate this influence to be as large as ±10° (see section 3.5 in ESI, Fig. S12 and S13†).

Microscopy. iPAINT images are acquired using a Nikon Eclipse Ti-E N-STORM system supplied by ∼488.0 mW cm^{-2} (λ = 561 nm) and ∼160.0 mW cm^{-2} (λ = 405 nm) laser lines set for *quasi*-TIRF imaging. The TIRF angle is adjusted to maximize the signal-to-noise ratio. The fluorescence signal is collected through a Nikon 100×, 1.49 NA oil immersion objective and filtered by a quad-band pass dichroic mirror (97335 Nikon). The region of interest used to acquire the time-lapses is set to 256 × 256 pixels of an ixon3, Andor EMCCD camera (pixel size 17 μm) at a frame rate of 47 frames per s. The adsorption of the iPAINT probes at the fluid interfaces is collected over 5 × 10^4 frames in each acquisition; the PEG-552 probes are continuously photo-activated with a low power UV laser (405 nm, 0.5% power), excited and subsequently bleached using a 561 nm laser (100% power). Single-molecule localization movies are analysed with NIS-element Nikon software.

Conclusions

In this work, we present the design of an innovative and complementary method based on super-resolution microscopy to image colloidal particles and fluid interfaces simultaneously and *in situ*. Through the continuous and non-covalent physisorption of polymer-conjugated photoactivatable dyes onto interfaces, we investigate the wetting properties of single hydrophobic and hydrophilic colloidal particles at a liquid–liquid interface, with a spatial resolution <20 nm. From iPAINT images, contact angle distributions and mean contact angles are determined, clearly showing a size-dependence of θ. Using the modified Young–Dupré equation, we account for this size dependence by calculating effective line tension forces exerted on the particles in the nanoNewton range. The possibility to follow the contour of the interface with high spatial resolution encouraged us to investigate further the interfacial deformations caused by the adsorption of anisotropic particles. iPAINT imaging of ellipsoidal colloids at decane–water interfaces shows the interface dipping at the tips and rising along the sides of the particles, confirming earlier theoretical computations on bigger ellipsoids. The minimally invasive and simultaneous imaging of interfaces and particles combined with its high spatial resolution makes iPAINT microscopy the ideal candidate to interrogate *in situ* phenomena connected to particles at interfaces. In particular, we hope to address further questions concerning the specific role of particle's size, shape and surface properties, which are essential to provide a full understanding of the assembly of particles at fluid interfaces.

Conflicts of interest

There are no conflicts to declare.

Acknowledgements

Notes and references

1 R. G. Alargova, D. S. Warhadpande, V. N. Paunov and O. D. Velev, *Langmuir*, 2004, **20**, 10371.

2 B. Madivala, S. Vandebril, J. Fransaer and J. Vermant, *Soft Matter*, 2009, **5**, 1717–1727.

3 T. M. Ruhland, A. H. Gröschel, N. Ballard, T. S. Skelhon, A. Walther, A. H. E. Müller and S. A. F. Bon, *Langmuir*, 2013, **29**, 1388–1394.

4 A. San-Miguel and S. H. Behrens, *Langmuir*, 2012, **28**, 12038–12043.

5 M. Zanini, C. Marschelke, E. S. Anachkov, E. Marini, A. Synytska and L. Isa, *Nat. Commun.*, 2017, **8**, 15701.

6 M. Zanini, I. Lesov, E. Marini, C.-P. Hsu, C. Marschelke, A. Synytska, S. E. Anachkov and L. Isa, *Langmuir*, 2018, **34**, 4861–4873.

7 A. Rauh, M. Rey, L. Barbera, M. Zanini, M. Karg and L. Isa, *Soft Matter*, 2017, **13**, 158–169.

8 R. W. Style, L. Isa and E. R. Dufresne, *Soft Matter*, 2015, **11**, 7412–7419.

9 K. Geisel, L. Isa and W. Richtering, *Langmuir*, 2012, **28**, 15770–15776.

10 O. S. Deshmukh, D. van den Ende, M. A. Cohen Stuart, F. Mugele and M. H. G. Duits, *Adv. Colloid Interface Sci.*, 2015, **222**, 215–227.

11 V. Schmitt and V. Ravaine, *Curr. Opin. Colloid Interface Sci.*, 2013, **18**, 532–541.

12 M. Xiao, A. Xu, T. Zhang and L. Hong, *Front. Chem.*, 2018, **6**, 225.

13 S. U. Pickering, *J. Chem. Soc. Trans.*, 1907, **91**, 2001–2021.

14 W. Ramsden, *Proc. R. Soc. London*, 1903, **72**, 156–164.

15 A. D. Dinsmore, M. F. Hsu, M. G. Nikolaides, A. R. Bausch, M. Marquez and D. A. Weitz, *Science*, 2002, **298**, 1006–1009.

16 E. Bormashenko, *Curr. Opin. Colloid Interface Sci.*, 2011, **16**, 266–271.

17 E. M. Herzig, K. A. White, A. B. Schofield, W. C. K. Poon and P. S. Clegg, *Nat. Mater.*, 2007, **6**, 966–971.

18 J. C. Loudet and B. Pouligny, *Europhys. Lett.*, 2009, **85**, 28003.

19 J. C. Loudet and B. Pouligny, *Phys. Rev. Lett.*, 2006, **97**, 018304.

20 L. Isa, F. Lucas, R. Wepf and E. Reimhult, *Nat. Commun.*, 2011, **2**, 438.

21 B. P. Binks, L. Isa and A. T. Tyowua, *Langmuir*, 2013, **29**, 4923–4927.

22 S. Coertjens, P. Moldenaers, J. Vermant and L. Isa, *Langmuir*, 2014, **30**, 4289–4300.

23 J. Fung, R. W. Perry, T. G. Dimiduk and V. N. Manoharan, *J. Quant. Spectrosc. Radiat. Transfer*, 2012, **113**, 212–219.

24 A. Wang, W. B. Rogers and V. N. Manoharan, *Phys. Rev. Lett.*, 2017, **119**, 108004.

25 C. Snoeyink, S. Barman and G. F. Christopher, *Langmuir*, 2015, **31**, 891–897.

26 S. Cappelli, A. M. de Jong, J. Baudry and M. W. J. Prins, *Soft Matter*, 2016, **12**, 5551–5562.

27 S. Cappelli, A. M. de Jong, J. Baudry and M. W. J. Prins, *Langmuir*, 2017, **33**, 696–705.

28 C. J. Mable, N. J. Warren, K. L. Thompson, O. O. Mykhaylyk and S. P. Armes, *Chem. Sci.*, 2015, **6**, 6179–6188.

29 P. I. Pieranski, *Phys. Rev. Lett.*, 1980, **45**, 569–572.

30 F. Bresme and M. Ottel, *J. Phys.: Condens. Matter*, 2007, **17**, 413101.

31 T. M. Squires and T. G. Mason, *Annu. Rev. Fluid Mech.*, 2010, **42**, 413–438.

32 Y. Peng, W. Chen, T. M. Fischer, D. A. Weitz and P. Tong, *J. Fluid Mech.*, 2009, **618**, 243–261.

33 T. M. Fischer, P. Dhar and P. Heinig, *J. Fluid Mech.*, 2006, **558**, 451–475.

34 T. Cubaud and T. G. Mason, *Phys. Fluids*, 2008, **20**, 053302.

35 S. L. Anna, *Annu. Rev. Fluid Mech.*, 2016, **48**, 285–309.

36 V. N. Paunov, *Langmuir*, 2003, **19**, 7970–7976.

37 L. N. Arnaudov, O. J. Cayre, M. A. Cohen Stuart, S. D. Stoyanov and V. N. Paunov, *Phys. Chem. Chem. Phys.*, 2010, **12**, 328–331.

38 S. P. McBride and B. M. Law, *Phys. Rev. Lett.*, 2012, **109**, 196101.

39 B. M. Law, S. P. McBride, J. Y. Wang, H. S. Wie, G. Paneru, S. Betelu, B. Ushijima, Y. Takata, B. Flanders, F. Bresme, H. Matsubara, T. Takiue and M. Aratono, *Prog. Surf. Sci.*, 2017, **92**, 1–39.

40 M. Sabapathy, V. Kollabattula, M. G. Basavaraj and E. Mani, *Nanoscale*, 2015, 7, 13868–13876.

41 J. van Rijssel, M. van der Linden, J. D. Meeldijk and R. J. A. van Dijk-Moes, *Phys. Rev. Lett.*, 2013, **111**, 108302.

42 N. Vogel, J. Ally, K. Bley, M. Kappl, K. Landfester and C. K. Weiss, *Nanoscale*, 2014, **6**, 6879–6885.

43 A. Aloi and I. K. Voets, *Curr. Opin. Colloid Interface Sci.*, 2018, **34**, 59–73.

44 A. Aloi, N. Vilanova, L. Albertazzi and I. K. Voets, *Nanoscale*, 2016, **8**, 8712–8716.

45 A. Aloi, C. Guibert, L. L. C. Olijve and I. K. Voets, *Polymer*, 2016, **107**, 450–455.

46 B. Adelizzi, A. Aloi, N. J. Van Zee, A. R. A. Palmans, E. W. Meijer and I. K. Voets, *ACS Nano*, 2018, **12**, 4431–4439.

47 N. J. Van Zee, B. Adelizzi, M. F. J. Mabesoone, X. Meng, A. Aloi, R. H. Zha, M. Lutz, I. A. W. Filot, A. R. A. Palmans and E. W. Meijer, *Nature*, 2018, **558**, 100–103.

48 B. Adelizzi, A. Aloi, A. J. Markvoort, H. M. M. Ten Eikelder, I. K. Voets, A. R. A. Palmans and E. W. Meijer, *J. Am. Chem. Soc.*, 2018, **140**, 7168–7175.

49 A. Maestro, L. J. Bonales, H. Ritacco, R. G. Rubio and F. Ortega, *Phys. Chem. Chem. Phys.*, 2010, **12**, 14115–14120.

50 D. M. Kaz, R. McGorty, M. Mani, M. P. Brenner and V. N. Manoharan, *Nat. Mater.*, 2012, **11**, 138–142.

51 M. Zanini and L. Isa, *J. Phys.: Condens. Matter*, 2016, **28**, 313002.

52 A. Maestro, E. Guzmán, F. Ortega and R. G. Rubio, *Curr. Opin. Colloid Interface Sci.*, 2014, **19**, 355–367.

53 M. Shao, J. Wang and X. Zhou, *Sci. Rep.*, 2015, **5**, 9491.

54 J. H. Weijs, A. Marchand, B. Andreotti, D. Lohse and J. H. Snoeijer, *Phys. Fluids*, 2011, **23**, 022001.

55 H. Lehle, E. Noruzifar and M. Ottel, *Eur. Phys. J. E: Soft Matter Biol. Phys.*, 2008, **26**, 151–160.

56 M. Oettel and S. Dietrich, *Langmuir*, 2008, **24**, 1425–1441.

57 J. Vermant, *Nature*, 2011, **476**, 286–287.

58 J. C. Loudet, A. M. Alsayed, J. Zhang and A. G. Yodh, *Phys. Rev. Lett.*, 2005, **94**, 018301.

59 S. Dasgupta, M. Katava, M. Faraj, T. Auth and G. Gompper, *Langmuir*, 2014, **30**, 11873–11882.

60 L. Botto, E. P. Lewandowski Jr., M. Cavallaro and K. J. Stebe, *Soft Matter*, 2012, **8**, 9957–9971.

61 G. B. Davies, T. Krüger, P. V. Coveney, J. Harting and F. Bresme, *Adv. Mater.*, 2014, **26**, 6715–6719.

62 S. Lou, X. Jiang and P. J. Scott, *Proc. R. Soc. A*, 2013, **469**, 20130150.

63 G. B. Davies and L. Botto, *Soft Matter*, 2015, **11**, 7969–7976.

64 G. B. Davies, T. Krüger, P. V. Coveney, J. Harting and F. Bresme, *Soft Matter*, 2014, **10**, 6742–6748.

65 N. Vilanova, I. de Feijter and I. K. Voets, *J. Visualized Exp.*, 2016, **110**, e53934.

66 A. K. van Helden, J. W. Jansen and A. Vrij, *J. Colloid Interface Sci.*, 1981, **81**, 354–368.

67 K. M. Keville, E. I. Franses and J. M. Caruthers, *J. Colloid Interface Sci.*, 1991, **144**, 103–126.